Nucleic Acids Research, 2024, **52**, 2711–2723
https://doi.org/10.1093/nar/gkae036
Advance access publication date: 28 January 2024
Structural Biology

Structural insights into the HDAC4–MEF2A–DNA complex and its implication in long-range transcriptional regulation

Shuyan Dai[1,2,†], Liang Guo[3,†], Raja Dey[4,†], Ming Guo[1], Xiangqian Zhang[1], Darren Bates[3], Justin Cayford[4], Longying Jiang[1], Hudie Wei[1], Zhuchu Chen[1], Ye Zhang[1,*], Lin Chen[4,*] and Yongheng Chen[1,*]

[1]Department of Oncology, NHC Key Laboratory of Cancer Proteomics & State Local Joint Engineering Laboratory for Anticancer Drugs, National Clinical Research Center for Geriatric Disorders, Xiangya Hospital, Central South University, Changsha, Hunan 410008, China
[2]Department of Pharmacology, Xiangya School of Pharmaceutical Sciences, Central South University, Changsha 410078, China
[3]Department of Chemistry and Biochemistry, University of Colorado, Boulder, CO 80309-0215, USA
[4]Molecular and Computational Biology, Department of Biological Sciences, University of Southern California, Los Angeles, CA 90089, USA

[*]To whom correspondence should be addressed. Tel: +86 731 84327542; Fax: +86 731 84327542; Email: yonghenc@163.com
Correspondence may also be addressed to Lin Chen. Tel: +1 213 8214277; Fax: +1 213 7408631; Email: linchen@usc.edu
Correspondence may also be addressed to Ye Zhang. Tel: +86 731 84327542; Fax: +86 731 84327542; Email: yezhang90@163.com
[†]The authors wish it to be known that, in their opinion, the first three authors should be regarded as Joint First Authors.

Abstract

Class IIa Histone deacetylases (HDACs), including HDAC4, 5, 7 and 9, play key roles in multiple important developmental and differentiation processes. Recent studies have shown that class IIa HDACs exert their transcriptional repressive function by interacting with tissue-specific transcription factors, such as members of the myocyte enhancer factor 2 (MEF2) family of transcription factors. However, the molecular mechanism is not well understood. In this study, we determined the crystal structure of an HDAC4–MEF2A–DNA complex. This complex adopts a dumbbell-shaped overall architecture, with a 2:4:2 stoichiometry of HDAC4, MEF2A and DNA molecules. In the complex, two HDAC4 molecules form a dimer through the interaction of their glutamine-rich domain (GRD) to form the stem of the 'dumbbell'; while two MEF2A dimers and their cognate DNA molecules are bridged by the HDAC4 dimer. Our structural observations were then validated using biochemical and mutagenesis assays. Further cell-based luciferase reporter gene assays revealed that the dimerization of HDAC4 is crucial in its ability to repress the transcriptional activities of MEF2 proteins. Taken together, our findings not only provide the structural basis for the assembly of the HDAC4–MEF2A–DNA complex but also shed light on the molecular mechanism of HDAC4-mediated long-range gene regulation.

Graphical abstract

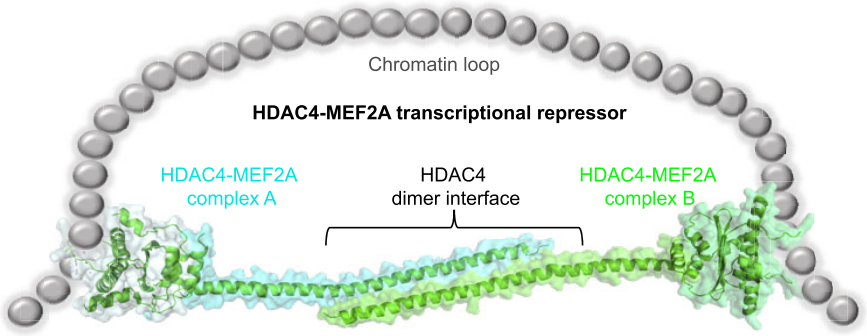

Introduction

Histone deacetylases (HDACs) are important epigenetic modifiers. As their name infers, the primary function of HDACs is to catalytically remove the posttranslational acetyl modifications from histones (1). The deacetylation of histones by HDACs usually induces a compact nucleosome conformation and downregulates transcription levels (2,3). The human genome encodes 11 HDAC proteins and can be further divided into four subgroups (Class I, IIa, IIb and IV) based on their sequence homology (1).

Class IIa HDACs, including HDAC4, 5, 7 and 9, are critical regulators in developmental and differentiation processes. Class IIa HDACs are characterized by tissue-specific expression behavior and can shuttle between the nucleus and cytoplasm (4). Compared to other HDACs, class IIa HDACs are relatively large proteins (120–135 kDa) with an extended

Received: July 27, 2023. **Revised:** December 1, 2023. **Editorial Decision:** January 4, 2024. **Accepted:** January 10, 2024

N-terminal domain and only have weak deacetylase activity (4–6). It has been suggested that the transcriptional repressive function of class IIa HDACs is independent of the C-terminal deacetylase domain (7,8). Instead, class IIa HDACs can interact directly with tissue-specific transcription factors, such as members of the myocyte enhancer factor 2 (MEF2) family of transcription factors, to repress gene transcription (9).

The HDAC–MEF2 axis has been implicated in diverse biological processes, including differentiation, tissue morphogenesis, and adaptive responses (10–12). Dysfunction of class IIa HDACs and MEF2 transcription factors has been frequently observed in different cancers (13–16). Class IIa HDACs contain a conserved N-terminal glutamine-rich domain (GRD) that can bind and repress the transcriptional activity of MEF2 proteins. Previous studies revealed that the C-terminal end of class IIa HDAC GRD folds into an amphipathic helix that binds to the MADS-box/MEF2s domain of MEF2 (17–21). The majority of glutamine-rich sequences fold into a long helix that dynamically equilibrates between dimer and tetramer (17,22). These observations highlighted the possibility that the HDAC–MEF2 axis functions in a high-order complex. Indeed, increasing evidence has shown that the MEF2–HDAC repression complex organizes in an oligomerization state and implicates long-range gene regulation (23–25).

Long-range genomic contacts between distal regulatory elements are important for diverse nuclear processes, especially in gene regulation (26–30). Genome-wide analyses of MEF2 binding sites in Drosophila by ChIP-on-chip reveal that MEF2 binds an unexpectedly large number of sites throughout the genome and that many genes have multiple MEF2 sites scattered in their promoter regions (31). These observations imply that the HDAC–MEF2 complex may exert a strong effect on chromosome construction and gene regulation. However, the underlying molecular basis has not been fully elucidated. In this paper, we aim to address this question by combining crystallographic and biochemical assays.

Materials and methods

Protein expression and purification

The genes encoding human HDAC4 GRD ($HDAC4_{GRD}$ residues 62–192) and MEF2A (1–95, $MEF2A_{1–95}$) were amplified by polymerase chain reaction (PCR) and subsequently subcloned into a pET-28a expression vector (Novagen, USA), respectively. Recombinant proteins were overexpressed in Escherichia coli BL21 (DE3) pLysS (Stratagene, La Jolla, CA, USA). Cells were grown at 37°C in 2× YT culture medium, induced with 0.5 mM IPTG when the culture OD_{550} reached 0.6, and then further cultured at room temperature for 6 hours. Cells were harvested by centrifugation at 4000 rpm for 15 min. For protein purification, cells were resuspended and homogenized by sonicating in a buffer containing 30 mM HEPES pH 7.5, 250 mM NaCl and 10 mM imidazole. The cell lysate was further clarified by centrifugation at 16 000 rpm for 30 min. Then, the supernatant was subjected to nickel-affinity chromatography and subsequently treated with thrombin protease to remove fusion tags, followed by ion exchange and size exclusion chromatography for further purification. Purified proteins were stored in a buffer containing 20 mM HEPES pH 7.5, 250 mM NaCl and 0.5 mM TCEP.

Site-directed mutagenesis was obtained by PCR with the wild-type $HDAC4_{GRD}$ plasmid used as the template and confirmed by DNA sequencing. The purification of $HDAC4_{GRD}$ mutants was conducted following the same steps as the WT protein.

Duplex DNA preparation

All single-stranded DNA oligonucleotides were purchased from Genewiz (Suzhou, China) and further purified by ion exchange. DNA duplexes were generated by annealing as described previously (32). The 28 bp DNA 5′-GGGAAAGTTTCTATTATTAGCAGAGATA-3′ (underlined nucleotides indicate the core MEF2 binding motif) used for the electrophoretic mobility shift assay (EMSA) was annealed to 45 μM. The 15 bp DNA 5′-AAACTATTTATAAGA-3′ used for crystallization was annealed to a concentration of 2 mM.

Crystallization and data collection

The $HDAC4_{GRD}$–$MEF2A_{1–95}$–DNA complex was prepared by mixing $HDAC4_{GRD}$, $MEF2A_{1–95}$ and the 15 bp DNA duplex at a molar ratio of 1:2:1.2. The final concentrations of the three components were 0.3, 0.6 and 0.36 mM, respectively. Crystals were obtained by the hanging-drop vapor diffusion method under the condition of 50 mM HEPES pH 7.5, 0.2 M NaCl, 3% (v/v) PEG 4000 at 20°C. Crystals were grown to full size within 10 days and flash-frozen in liquid nitrogen after treatment with cryoprotectant buffer consisting of reservoir solution plus 20% (v/v) glycerol and 10% (v/v) ethylene glycol. Diffraction data were collected at beamline 8.2.1 of the Advanced Light Source (ALS).

Data processing, structure determination and refinement

The diffraction data were processed using the HKL2000 software suite (33). The structure was determined by molecular replacement (MR) under the program Phenix.Phaser (34), with the HDAC9–MEF2B–DNA (PDB code: 1TQE) (20) and apo $HDAC4_{GRD}$ (PDB code: 2H8N) (17) structures used as search templates. After initial phases were determined by MR, rigid body refinements were performed to better determine the non-crystallographic symmetry constraints (NCS). Subsequently, several rounds of torsional angle dynamics, NCS, and grouped B factor refinement were carried out, resulting in a model with an R_{free} value of 38%. Phases calculated from this model was further improved using non-crystallographic symmetry averaging, solvent flattening, and histogram matching with DM (35). Using the improved phases, $F_o - F_c$ maps were calculated and used to build the missing $HDAC4_{GRD}$ residues 130–166 in Coot (36). The final structure model, with an R_{work}/R_{free} of 26%/30%, was obtained after several cycles of LORESTR refinement (37), manual rebuilding, and Phenix.Refine (38). Data processing and structure refinement statistics are summarized in Supplementary Table S1.

EMSA

EMSA was performed as described previously (39). In brief, reaction mixtures were prepared in a total volume of 10 μl with 20 mM HEPES pH 7.5, 200 mM NaCl, 10 mM $MgCl_2$, 1 mM EDTA, 0.1 mM DTT and 0.5% Triton X-100 used as an analysis buffer. $MEF2A_{1–95}$ and DNA were

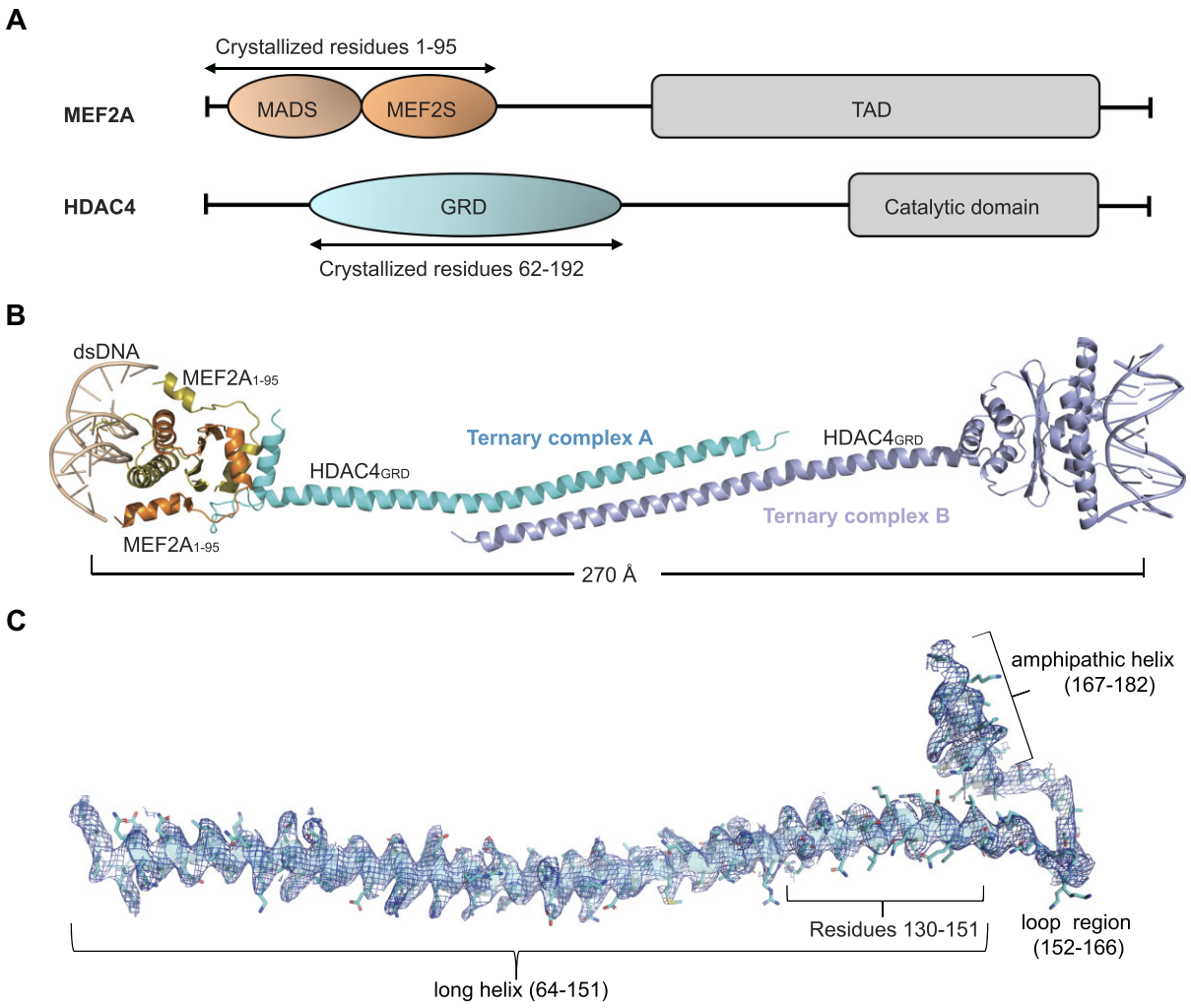

Figure 1. Overall structure of the $HDAC4_{GRD}$–$MEF2A_{1–95}$–DNA complex. (**A**) Schematic diagram of human MEF2A and HDAC4 proteins. The truncations used for crystallization are indicated. (**B**) Ribbon diagram of the $HDAC4_{GRD}$–$MEF2A_{1–95}$–DNA complex. (**C**) Structure of $HDAC4_{GRD}$. The $2F_o - F_c$ omit map is contoured at the 1.0 σ level.

mixed at a molar ratio of 2:1.2 with a final concentration of DNA of 1.2 μM. $HDAC4_{GRD}$ was supplied at gradient concentrations of 0.5, 1, 1.5 and 3 μM. Reaction mixtures were incubated on ice for at least 30 min before loading onto a 6% (w/v) native polyacrylamide gel. Electrophoreses were performed with 0.5× TBE used as a running buffer and visualized by using GoldView at a final concentration of 0.5 μg/ml.

Size exclusion chromatography (SEC)

SEC analyses were conducted using an ÄKTA Pure (GE Healthcare, USA) and a Superdex 200 10/300 GL column at 16°C. The column was pre-equilibrated with a SEC buffer (20 mM HEPES, pH 7.5, 200 mM NaCl and 2 mM DTT), and then calibrated with premixed protein standards, including ribonuclease A (13.7 kDa), carbonic anhydrase (29 kDa) and ovalbumin (44 kDa) (GE Healthcare, USA). The chromatographic profiles of $HDAC4_{GRD}$ proteins (WT, F93D and H109D) were measured by injecting 500 μl of protein sample at a concentration of 50 μM. Due to the absence of Trp, Tyr, or Cys residues in the recombinant $HDAC4_{GRD}$ proteins, curves were recorded at UV absorbance at 230 nm (A_{230}) instead of A_{280}. Data were processed and presented using Origin 8.

Co-immunoprecipitation (Co-IP) and western blotting

HEK293T cells were transfected with Flag-$HDAC4^{WT}$, Flag-$HDAC4^{H109D}$ or Flag-$HDAC4^{F93D}$, along with Myc-HDAC4, and cultured for an additional 24 h. For anti-Flag immunoprecipitation, cells were lysed in a 0.3% NP40 buffer containing inhibitors (1 mM phenylmethylsulphonyl fluoride, 1 mg/ml of aprotinin, 1 mg/ml of leupeptin, 1 mg/ml of pepstatin, 1 mM Na_3VO_4, 1 mM NaF, all in their final concentrations). Debris was removed by centrifugation at 4°C, 12 000 rpm for 15 min. The cell lysates were then incubated with anti-flag M2-agarose (Sigma) overnight at 4°C. The immunoprecipitates were washed thrice with lysis buffer, boiled, loaded into a denaturing polyacrylamide gel, separated by SDS-PAGE, and transferred to a PVDF membrane (Millipore). The membrane was blocked with 5% milk, washed with PBST buffer (500 ml 1 × PBS buffer with 1 ml Tween-20, pH 7.5), and incubated with appropriate antibodies. The MYC antibody (Immunoway, YM3002) was used at a 1:1000 working dilu-

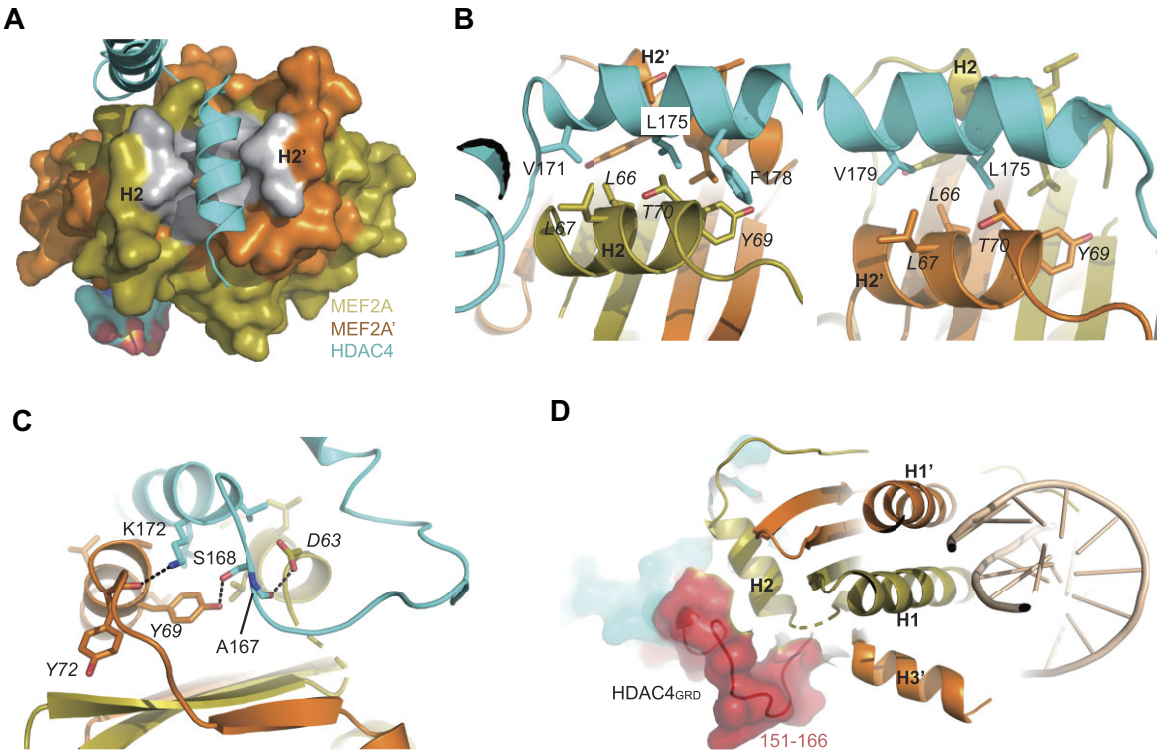

Figure 2. HDAC4–MEF2A interactions. (**A**) Surface presentation of the HDAC-binding cleft formed by the MEF2A$_{1–95}$ homodimer. Residues that contributed to shaping the binding groove are colored gray. (**B**) Hydrophobic interactions between HDAC4$_{GRD}$ and MEF2A$_{1–95}$ are shown in two views. Interaction residues are shown in sticks. (**C**) H-bond interactions present in the HDAC4$_{GRD}$–MEF2$_{1–95}$ interaction interface. H-bonds are indicated by dashed lines and defined at a distance cutoff of 3.5 Å. (**D**) The interaction interface contributed by HDAC4 residues outside its MEF2-binding motif. HDAC4 is shown in surface representation with the MEF2-binding motif hidden for clarification. The MEF2A binding interface of HDAC4 is highlighted in red.

tion, the Flag antibody (Sigma, F7425) was used at a 1:1000 working dilution, and the secondary antibodies (Proteintech, SA00001) were commercially obtained. Finally, the ECL substrate (Biosharp, BL520A) was applied to the membranes and the results were scanned by G:BOX Chemi XX9.

DNA bridging assay

For the DNA bridging assay, two DNA duplexes, Site-1 (forward sequence: 5′-GGGAAAGTTTCTATTATTAGCAGAGATA-3′) and Site-2 (5′-CTAAGCAAATGAGATGAATATGCAGGGCACCATGCTAAAAATAAAATGGTTTCATGGTGCTAGTGAGGAAGGAA-3′), were synthesized. The 5′ end of the forward chain of Site-1 DNA was synthesized with a biotin label. The pull-down experiment was conducted as follows: 10 pmol Site-1 DNA was bound to 10 μl Streptavidin MagBeads (GenScript, Cat. No. L00424) according to the reaction conditions following the manufacturer's recommendation; the beads were blocked with 5% BSA and 1 μM T7 primers; the beads were washed thrice with binding buffer (5 mM Tris pH 7.4, 0.5 mM EDTA, 250 mM NaCl); immobilized Site-1 DNA was mixed with recombinant proteins (HDAC4$_{GRD}$ and MEF2A$_{1–95}$) and 2 pmol Site-2 DNA, and further incubated at 4°C for 1 h; the beads were washed 8 times, and Site-2 DNA was released by boiling in pure water containing 0.1% SDS. The enrichment of Site-2 was detected by qPCR using the SYBR green system with the following primers: 5′-CTAAGCAAATGAGATGAATATGCA-3′ and 5′-TTCCTTCCTCACTAGCACCATG-3′.

Atomic force microscope (AFM)

The 1040 bp AFM DNA was obtained through PCR amplification using the *Homo sapiens* aryl hydrocarbon receptor interacting protein cDNA (NCBI accession number: NM_003977) as a template. The primers used were 5′-CAGGGAAAGTTTCTAAAAATAGCAATGGCGGATATCATCGCAAGACTCCG-3′ and 5′-GTAGGTATCTCTGCTATTTTTAGTCAATGGGAGAAGATCCCCCGGAAC-3′ (underlined nucleotides indicate the core MEF2 binding motif). For the DNA alone AFM sample, 20 μl of 4 ng/μl DNA in a buffer containing 20 mM Tris–HCl pH 7.5, 50 mM NaCl, 2.5 mM DTT and 2.5 mM $MgCl_2$ was deposited onto a newly cleaved mica surface. To obtain the AFM sample of MEF2A$_{1–95}$-bound DNA, MEF2A$_{1–95}$ protein was supplied to the 4 ng/ul DNA at a final concentration of 4 nM and further incubated for 20 minutes before being deposited onto the mica surface. To obtain the HDAC4$_{GRD}$–MEF2A$_{1–95}$–DNA complex, 4 nM HDAC4$_{GRD}$ was added to the MEF2A$_{1–95}$–DNA mixture and further incubated for 20 minutes before being deposited onto the mica surface. All micas were equilibrated for 10 minutes, then raised with 500 μl of MilliQ water and dried with nitrogen gas.

AFM images were collected at a Dimension Icon AFM (Bruker) in a ScanAsyst mode in air, using a SCANASEYST-AIR cantilever (resonant frequency: 70 kHz; force constant: 0.4 N m^{-1}). The images were flattened and the contrast and brightness were adjusted for optimal viewing conditions with NanoScope Analysis V1.7 software.

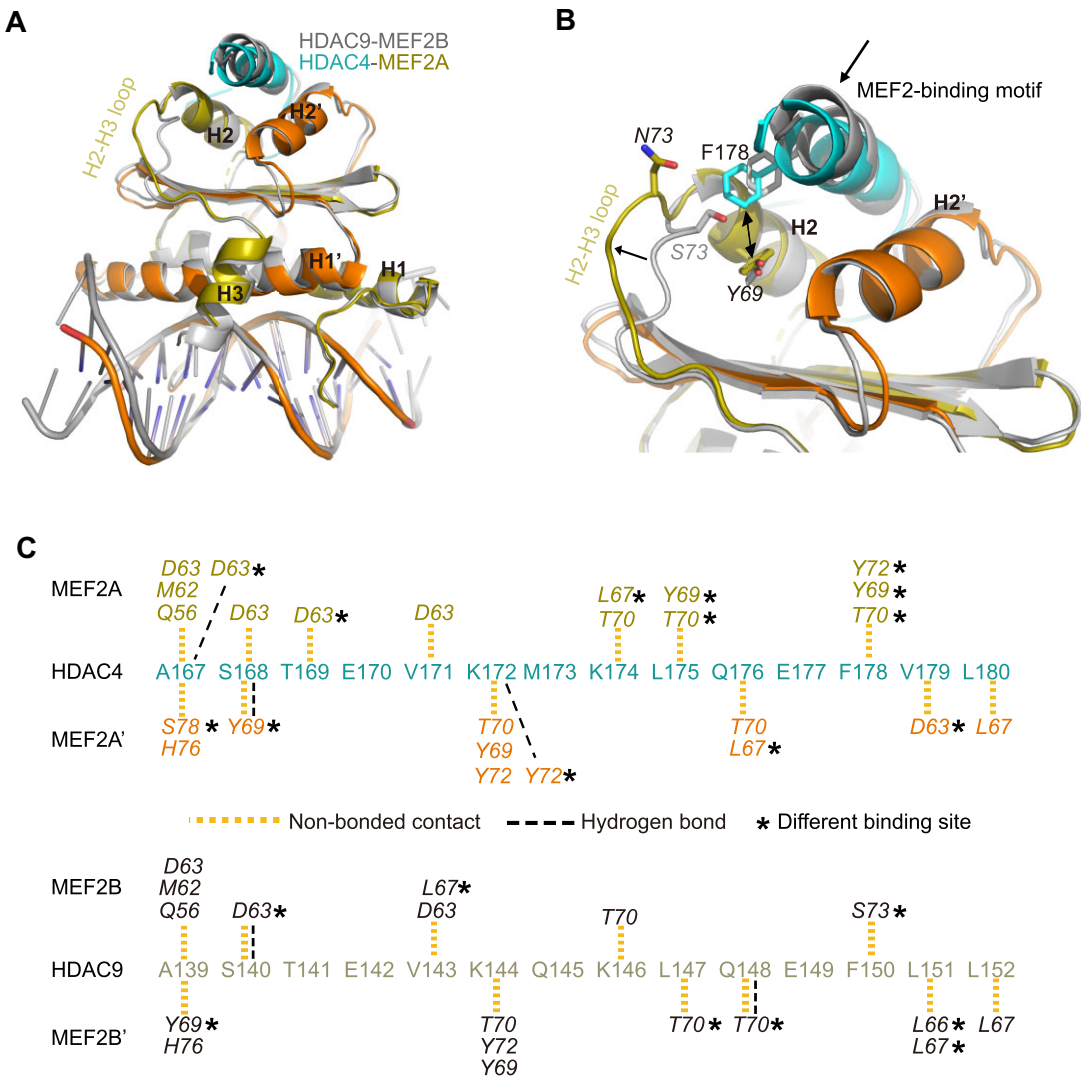

Figure 3. Structural comparison of the HDAC4–MEF2A and HDAC9–MEF2B complexes. (**A**) Superimposition of HDAC4–MEF2A–DNA and HDAC9–MEF2B–DNA (gray) complexes. Residues except for the MEF2-binding motif of HDAC4 were hidden for clarity. (**B**) Local structural differences present between the two compared structures. Significant conformation variants are indicated by arrows. (**C**) Schematic diagram of detailed HDAC–MEF2 interactions between the two structures.

Luciferase reporter gene assay

HEK293T cells were seeded in 12-well plates and further cultured overnight. The cells were then transfected with 500 ng of pcDNA–HDAC4^{WT} or pcDNA–HDAC4^{mut}, 1000 ng of pGL3-3xMEF2s–Luc (containing three tandem MEF2 binding motifs), and 200 ng of pRL-TK (control Renilla luciferase). After 24 h of transfection, luciferase activity was measured using the dual-luciferase reporter assay kit (Beyotime, RG027) by following the manufacturer's instructions. Firefly luciferase activity values were normalized to the Renilla luciferase activity to reflect expression efficiency. The experiments were performed in triplicate and repeated four times. Data were analyzed using Microsoft Excel and plotted with Prism 7 (GraphPad Software).

Results

Overall structure of the HDAC4$_{GRD}$–MEF2A$_{1–95}$–DNA complex

To elucidate how the MEF2–HDAC repressive complex is assembled, we purified the GRD of HDAC4 (HDAC4$_{GRD}$) and the MADS-box/MEF2s domain of MEF2A (MEF2A$_{1–95}$) and co-crystallized these two proteins in the presence of a 15-mer DNA duplex that possesses a MEF2A binding site (Figure 1A). The complex structure was determined by molecular replacement and refined to a resolution of 3.6 Å with an R_{work}/R_{free} of 0.26/0.30 (Supplementary Table S1). The crystal asymmetric unit (ASU) contains two copies of the HDAC4$_{GRD}$–MEF2A$_{1–95}$–DNA complex, which is formed by the three components at a stoichiometry of 1:2:1 (Figure 1B). HDAC4$_{GRD}$ bound to dimeric MEF2A$_{1v95}$ through an amphipathic helix similar to observations in the Cabin1vMEF2B and HDAC9–MEF2B structures (20,40). Interestingly, the structure showed that the two nearly identical HDAC4$_{GRD}$–MEF2A$_{1–95}$–DNA complexes in ASU were further dimerized through coiled-coil interactions mediated by HDAC4$_{GRD}$. The two HDAC4$_{GRD}$–MEF2A$_{1–95}$–DNA complexes dimerized and assembled into an ∼270 Å dumbbell-like shape, where the HDAC4$_{GRD}$ helix dimer formed the stem of the 'dumbbell', and two MEF2A$_{1–95}$ dimers and their cognate DNA molecules were bridged by the HDAC4$_{GRD}$ dimer (Figure 1B).

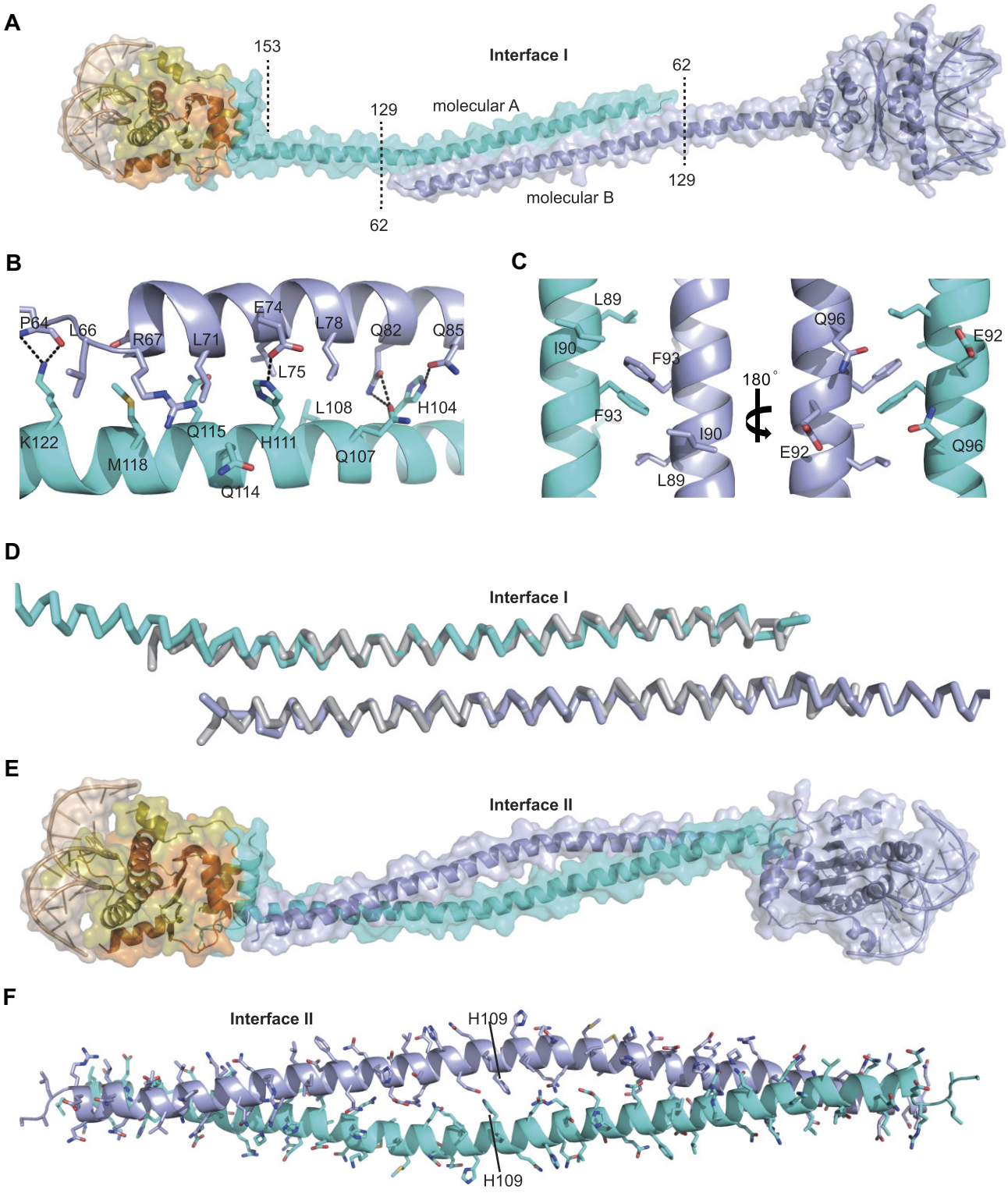

Figure 4. HDAC4 dimer interface. (**A**) Surface presentation of $HDAC4_{GRD}$ dimer interface I. Residues involved in dimerization are indicated. (**B**) 'Knob-into-hole' interactions present in the $HDAC4_{GRD}$ dimer interface. H-bonds are indicated by dashed lines. (**C**) Hydrophobic core formed in Interface I. Residues that engaged in the hydrophobic core are shown in sticks. (**D**) Superposition of dimer interface I and the same dimer interface observed in the apo $HDAC4_{GRD}$ structure (gray, PDB entry: 2H8N). (**E**) $HDAC4_{GRD}$ dimer interface II in the crystal lattice. (**F**) Interactions presented in interaction interface II.

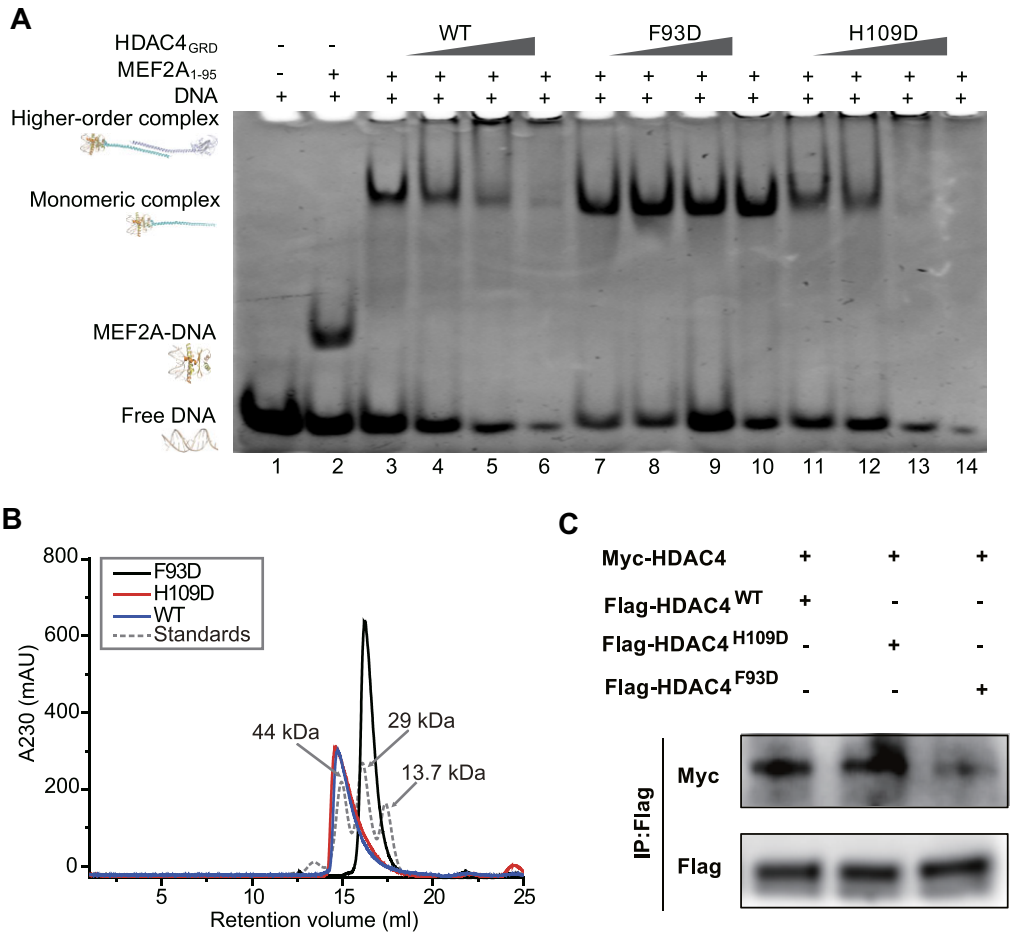

Figure 5. Characterization of the HDAC4–MEF2A–DNA complex. (**A**) EMSA migration profile of $HDAC4_{GRD}$–$MEF2A_{1–95}$–DNA complexes formed by different $HDAC4_{GRD}$ mutants. DNA and $MEF2A_{1–95}$ were supplied at constant concentrations of 1.2 and 2 μM, respectively. The concentration of $HDAC4_{GRD}$ was applied in a serially diluted concentration from 0.5 to 3 μM. (**B**) SEC profiles of different $HDAC4_{GRD}$ proteins on a Superdex 200 10/300 GL column. Curves were recorded at the UV absorbance of 230 nm. (**C**) Interaction between full-length myc-HDAC4 and different Flag-HDAC4 proteins. HEK293 cells were co-transfected with myc-HDAC4 and one of the Flag-HDAC4 proteins (WT, F93D and H109D). Immunoprecipitation was performed using anti-Flag antibody, and the precipitates were subjected to WB analysis. Blots were probed with anti-Flag or anti-Myc antibody.

Although the diffraction was limited to 3.6 Å, HDAC4 residues (64–183) could be contiguously built in the final structure model (Figure 1C). From the N- to C-terminus, $HDAC4_{GRD}$ can be divided into three parts: the long helix (residues 64–151), the loop region (residues 152–166), and the amphipathic MEF2-binding helix (residues 167–182) (Figure 1C). Surprisingly, amino acids 130–151 of HDAC4 were shown to be disordered in our previous biochemical and structural studies (17), whereas these residues fold into a helix in the structure determined here. This helix is observed at both $HDAC4_{GRD}$ copies in the ASU; therefore, it is unlikely to be an artifact caused by crystallization. Our observations suggested that $HDAC4_{GRD}$ may undergo conformational changes during HDAC4–MEF2 assembly.

HDAC4–MEF2A interaction interface

The interactions between HDAC4 and MEF2A share common features with those of previously reported Cabin1–MEF2B and HDAC9–MEF2B complexes (20,40). In binding to MEF2A, $HDAC4_{GRD}$ lies its MEF2-binding helix on a hydrophobic cleft supplied by the $MEF2A_{1–95}$ dimer (Figure 2A). The HDAC4 binding cleft was formed by *L66*, *L67*, *Y69* and *T70* from both $MEF2A_{1–95}$ H2 helixes (residues from MEF2A are italicized throughout the text). The hydrophobic interactions are primarily contributed by HDAC4 residues V171, L175, F178 and V179 of the amphiphilic helix (Figure 2B). Several hydrogen bonds (H-bonds) formed between $HDAC4_{GRD}$ and $MEF2A_{1–95}$ have also been observed. These H-bond interactions are formed by amino acid residue pairs K172/*Y72*, S168/*Y69* and A167/*D63* (Figure 2C). MEF2A residue *Y69* plays dual roles in interacting with HDAC4. In the MEF2A dimer, one *Y69* utilizes its side chain benzene ring to form a face-to-edge interaction with HDAC4 F178, while the other *Y69* forms an H-bond with HDAC4 S168 through its hydroxy oxygen (Figures 2B, C). The dual role of MEF2A *Y69* well-explains the observation that once the same tyrosine of MEF2B (also *Y69*) is mutated to alanine, MEF2B completely loses the ability to recruit HDAC4 *in vitro* (20).

In addition to interactions mediated by the MEF2-binding helix, the loop region (152–166) of $HDAC4_{GRD}$ also offered an additional ∼430 $Å^2$ interaction interface for MEF2A binding (Figure 2D). $HDAC4_{GRD}$ utilizes its residues L152, L155, K157, A165 and V166 to make extensive van der Waals interactions with the H2 and H3′ helices of the $MEF2A_{1–95}$ homodimer (Supplementary Figure S1). Furthermore, a salt

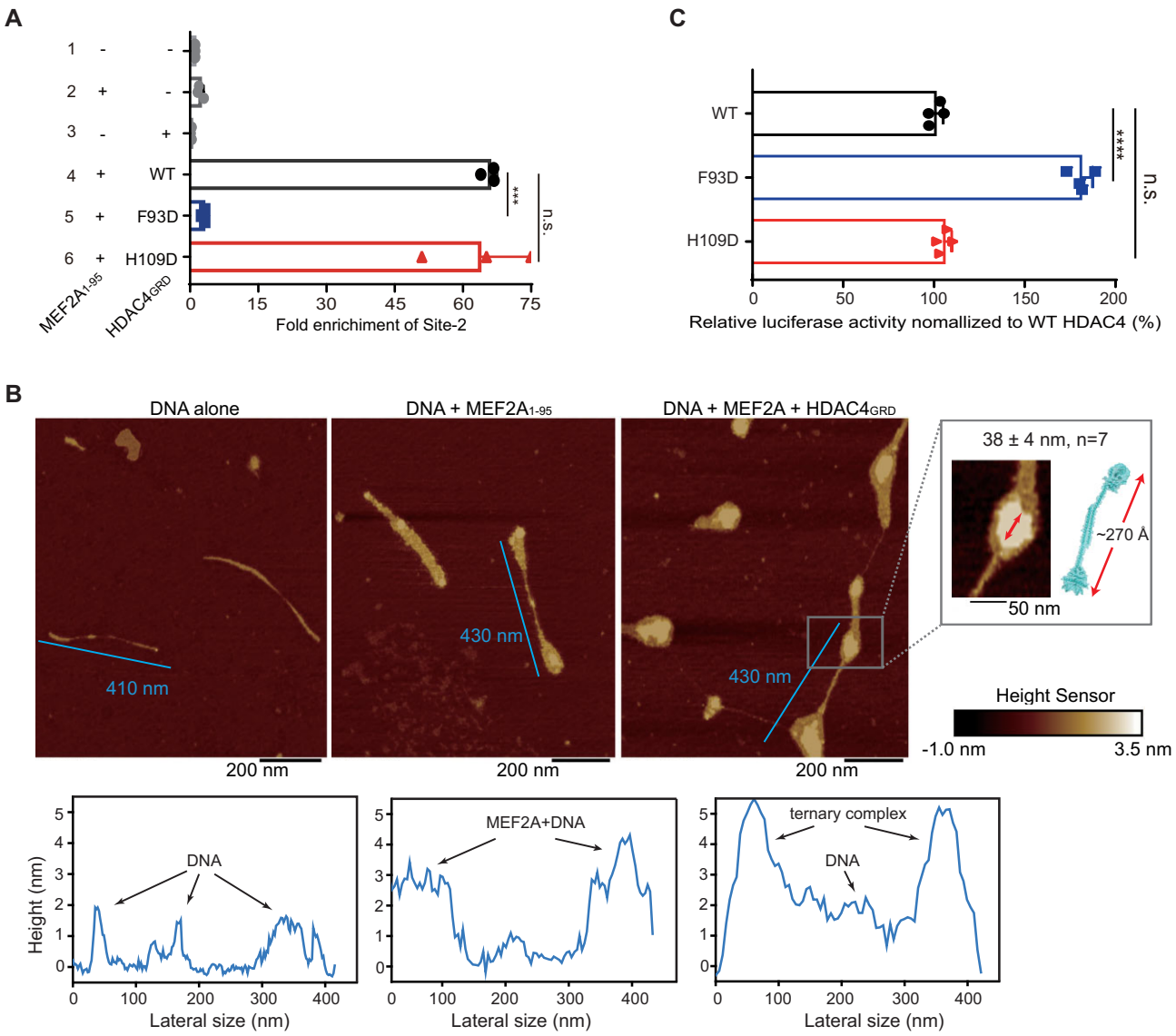

Figure 6. DNA bridging by the HDAC4–MEF2A complex. (**A**) Enrichment of Site-2 tested by DNA bridging assay. Folds of enrichment were quantified by qPCR. (**B**) AFM images of DNA morphology under different conditions (top panels). Bottom panels show the height profiles of the DNA chains as marked in the AFM images. As shown, the heights of the DNA, the DNA-bound MEF2A dimer, and the DNA-bound HDAC4–MEF2A complex are approximately 2, 4 and 5 nanometers, respectively. (**C**) Effects of HDAC4 mutations on the repression of transcriptional activities of MEF2 proteins. Data are shown the mean ± standard deviation of $n = 3$ (for B), and $n = 4$ (for C) independent replicates. *P* values were calculated using one-way ANOVA with Dunnett multiple comparisons test with the WT $HDAC4_{GRD}$ group as a control. ***$P < 0.001$, ****$P < 0.0001$, ns: not statistically significant ($P > 0.05$).

bridge formed between HDAC4 K156 and MEF2A *E71* could also be observed in this interaction interface (Supplementary Figure S1). These additional contacts may further stabilize the HDAC4–MEF2A interaction.

Structural comparison of HDAC4–MEF2A and HDAC9–MEF2B complexes

We then compared our structure with the previously determined HDAC9–MEF2B structure (20). The superimposition of these two structures gave a root mean square deviation (rmsd) of 0.3 Å, indicating that the two structures are very similar (Figure 3A). However, the orientations of local structural elements of MEF2 around the HDAC binding cleft, especially the loop between helices H2 and H3 (H2–H3 loop), showed notable differences (Figure 3B). In the $HDAC4_{GRD}$–$MEF2A_{1–95}$ structure, the H2–H3 loop flips away from the hydrophobic groove and points to the groove in the HDAC9–MEF2B structure (Figure 3B). The orientation of the MEF2A H2-H3 loop enabled a deeper insertion of the HDAC4 amphiphilic helix C-termini. Consequently, a much tighter interaction between the F178 and *Y69* side-chain benzene rings is observed (Figure 3B). The electronic density map shows that the difference is unlikely to be generated by the model bias we built (Supplementary Figure S2). Indeed, the H2–H3 loop of MEF2B has also been shown to adopt distinct conformations to bind different cofactors, and this plastic feature is thought to be a mechanism taken by MEF2 proteins to accommodate the binding of different cofactors (20,40).

In addition, detailed interactions between these two compared structures showed notable differences (Figure 3C). Both hydrophobic and H-bond contacts show some degree of rearrangement. For example, Q148 of HDAC9 forms an H-bond with MEF2B *T70*, while the corresponding glutamine

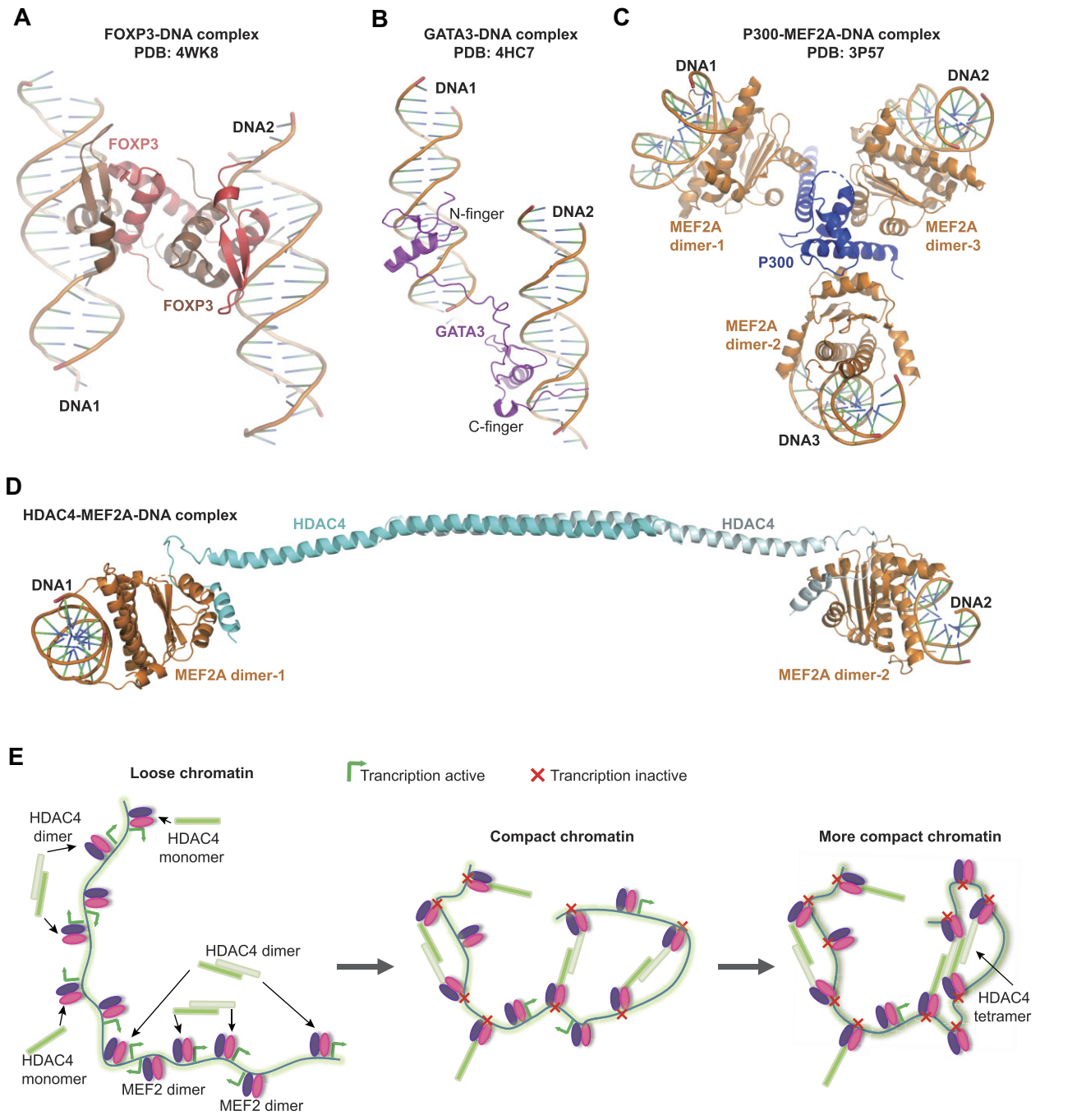

Figure 7. Different DNA bridging mechanisms adopted by different transcription factors. (**A**) The FOXP3 DNA binding domain forms a domain-swapped dimer to bind two distal DNA sites. (**B**) The GATA3 DNA binding domain contains two zinc fingers, with each finger binding one DNA molecule. The long linker present between the two zinc fingers may enable GATA3 to bind DNA sites at various distances. (**C**) A P300 protein binds three MEF2A–DNA complexes and assembles into an enhanceosome. (**D**) The dimeric HDAC4 binds two separate MEF2A–DNA complexes to repress gene transcription. (**E**) A hypothetical long-range transcriptional repression model by HDAC4. HDAC4 is recruited as a monomer or a dimer by MEF2 dimers to specific gene loci. The binding of HDAC4 leads to the transcriptional inactivation of target genes. The dimeric HDAC4 can bridge two gene sites, inducing a looped DNA conformation that may silence the transcription of genes located in the repression loop. The dimeric HDAC4–MEF2 complex may further form a tetramer or even higher-order complex, resulting in a more compact chromatin conformation and leading to a transcriptional inactive gene hub.

(Q176) does not contribute an H-bond interaction in the HDAC4–MEF2A structure; F178 of HDAC4 forms extensive hydrophobic interactions with MEF2A residues Y72, *Y69* and *T70*, whereas the corresponding phenylalanine contacts only MEF2B *S73* in the HDAC9–MEF2B structure (Figure 3C). While some of these differences may be caused by alternative crystal packing, the fact that the two copies of the MEF2 dimer in the symmetric unit displayed the same structural features suggests that most of the observed interaction differences are inherent to different HDAC–MEF2 interactions.

Helix dimer interface of HDAC4$_{GRD}$

Our structure showed that the long helix of HDAC4$_{GRD}$ further dimerizes and forms a head-to-tail stack (Figure 4A). PSIA (41) assigned this dimerization interface (Interface I) an ∼2767 Å^2 buried surface area formed by residues 62–129 of both HDAC4$_{GRD}$ molecules. The dimerization is mediated by typical coiled-coil interactions, which are characterized by regularly arranged non-polar residues and 'knob-into-hole' hydrophobic interactions. For example, M118 and H111 of one helix (helix A) and L71 and L78 of the other helix (helix B) act as 'knobs' and insert into the 'hole' formed by residues of each opposite helix. For instance, helix B L71 inserts into the 'hole' formed by M118, Q115, Q114 and H111 of helix A (Figure 4B). In addition to 'knob-into-hole' interactions, several H-bonds were also observed (Figure 4B). In the center of the dimer interface, a small hydrophobic core formed by L89, I90 and F93 from both chains is present (Figure 4C). As there is a 2-fold symmetry between the F93–F93 residue pair, the other side interactions in the dimer interface are identical. Although residues 130–151 further extended the long helix, this region does not contribute directly to dimerization.

The HDAC4$_{GRD}$ dimerization interface we reported here has also been observed in our previously reported apo HDAC4 tetramer structure (17) (Supplementary Figure S3A). The superimposition of these two HDAC4$_{GRD}$ dimers gave a rmsd of 1.45 Å for all 123 aligned Cα atoms, indicating that these two structures share almost an identical dimer interface (Figure 4D). However, we observed that hydrogen bonds formed between E92–Q96 residue pairs in the apo HDAC4$_{GRD}$ structure were absent in our structure (Supplementary Figure S3B), which might be due to model bias or resolution limitations. In addition, we did not observe other dimerization interfaces present in the apo HDAC4$_{GRD}$ tetramer in the structure we determined here (Supplementary Figure S3A).

In the crystal lattice, another potential HDAC4 dimerization interface (Interface II) can be observed (Figure 4E, and Supplementary Figure S3C). Interface II was contributed by the two entire long helixes (residues 64–153) of the HDAC4$_{GRD}$ dimer and had a buried surface area of 3735 Å^2. Similar to Interface I, in which the F93–F93 residue pair forms a πνπ stacking interaction, an H109–H109 stacking interaction has also been observed in the center of Interface II (Figure 4F). Although it has a larger interaction interface than Interface I, neither typical knob-into-hole interactions nor hydrophobic core was observed in Interface II (Figure 4F). These observations suggest that interface II may not be stable.

The HDAC4$_{GRD}$–MEF2A$_{1–95}$–DNA complex forms high-order oligomers in solution

To verify that the HDAC4$_{GRD}$–MEF2A$_{1–95}$–DNA complex can assemble into high-order oligomers in solution, we performed EMSAs to analyze the migration of the HDAC4$_{GRD}$–MEF2A$_{1–95}$–DNA complex. The complex migrated primarily as a monomer complex at a low HDAC4$_{GRD}$ concentration (Figure 5A, lane 3). However, once the HDAC4$_{GRD}$ concentration increased, the monomeric complex (one HDAC4$_{GRD}$ binds a MEF2A$_{1–95}$ dimer on one double-stranded DNA molecule) band became weak and could barely be detected at a high HDAC4$_{GRD}$ concentration (Figure 5A, lanes 4–6). Unexpectedly, the free DNA band also decreased alongside the complex when the HDAC4$_{GRD}$ concentration increased. No clear bands indicating higher-order complexes were seen on the gel but wells of the gel appeared to retain most of the materials of the binding reactions, suggesting that most of the protein/DNA complexes formed at high HDAC4$_{GRD}$ concentrations were unable to enter the gel matrix.

Mutating HDAC4$_{GRD}$ interface I residue disrupts its ability to form a dimeric HDAC4–MEF2A–DNA complex

To further clarify whether Interface I, Interface II, or both contribute to the dimerization of the HDAC4$_{GRD}$–MEF2A$_{1–95}$–DNA complex, we constructed HDAC4$_{GRD}$ F93D and H109D mutants and performed EMSAs. Compared to the wild-type (WT) HDAC4$_{GRD}$, the migration profile of F93D was dramatically different (Figure 5A, lanes 7–10). The mutation of F93 to aspartate abolished its ability to form a high-order complex, and only the monomeric complex band was observed (lanes 7–10). Furthermore, neither the migration of the complex nor the free DNA was impacted by the increase in F93D concentration. In contrast, H109D behaved almost identically to the WT protein (Figure 5A, lanes 11–14).

On the other hand, we also conducted size exclusion chromatography to examine the oligomeric state of HDAC4$_{GRD}$ in solution. Consistent with the EMSA results, WT and H109D HDAC4$_{GRD}$ exhibited similar profiles on a Superdex 200 column and were likely eluted as oligomers. Compared to WT and H109D, the elution peak of F93D was largely delayed and eluted as a monomer (18.2 kDa, with 6xhis tag), as determined by the retention curve of the standard mixtures (Figure 5B).

To verify that full-length HDAC4 also employs F93 to dimerize, we co-transfected HEK293T with full-length Myc-tagged HDAC4 and Flag-tagged HDAC4 (WT, F93D or H109D) and performed anti-Flag immunoprecipitation experiments. The results showed that Flag-HDAC4^{WT} and Flag-HDAC4^{H109D} could efficiently pull down myc-HDAC4, while Flag-HDAC4^{F93D} exhibited a comparatively weaker ability to immunoprecipitate Myc-HDAC4 (Figure 5C). These observations suggest that F93 plays a crucial role in mediating HDAC4 dimerization for both HDAC4$_{GRD}$ and the full-length protein.

The HDAC4$_{GRD}$–MEF2A$_{1–95}$ complex bridges two separate DNA sites in solution

As revealed by the structure, two separate DNA sites were bound simultaneously by the HDAC4$_{GRD}$–MEF2A$_{1–95}$ complex. However, SEC and EMSA experiments could not directly prove that two DNA sites were bridged in solution. To further clarify this observation, we performed a DNA bridging assay based on the pull-down and quantitative PCR technology (42). Two individual DNA sites were synthesized, with one site labeled by biotin at its 5′-end (Site-1) and the other

with qPCR extensions at both ends (Site-2). Site-1 was unable to enrich Site-2 in the presence of $MEF2A_{1–95}$ or $HDAC4_{GRD}$ alone, as quantified by qPCR (Figure 6A, lanes 2 and 3). When both WT $HDAC4_{GRD}$ and $MEF2A_{1–95}$ were supplied in the mixture, Site-2 was apparently accumulated (lane 4), indicating that $HDAC4_{GRD}$–$MEF2A_{1–95}$ could bind Site-1 and Site-2 simultaneously. Furthermore, apparent enrichment of Site-2 could not be observed when F93 was mutated to asparagine, whereas Site-2 similarly accumulated as WT $HDAC4_{GRD}$ by the H109D mutant (lanes 5 and 6). These results indicated that the $HDAC4_{GRD}$–$MEF2A_{1–95}$ complex could bridge two DNA sites in solution and demonstrate again that F93 plays an essential role in the dimerization of the complex.

To further demonstrate the DNA bridging ability of the $HDAC4_{GRD}$–$MEF2A_{1–95}$ complex, we performed AFM scanning to visualize the overall shape of the DNA in the presence of $HDAC4_{GRD}$. Interestingly, in the presence of $HDAC4_{GRD}$, the $MEF2A_{1–95}$–DNA complexes were tandemly linked and assembled into a bracelet-like shape (Figure 6B). On the contrary, in the absence of $HDAC4_{GRD}$, this DNA-tandem phenomenon is neither observed in the DNA alone nor the $MEF2A_{1–95}$–DNA AFM sample (Figure 6B). These results indicated that the $MEF2A_{1–95}$–DNA complexes could be bridged by $HDAC4_{GRD}$*in vitro*.

The dimerization of HDAC4 is essential in suppressing the transcriptional activities of MEF2 proteins

Biochemical assays and AFM imaging have shown that HDAC4 is capable of forming a dimer or higher oligomer when binds to the MEF2A–DNA complex. To investigate the biological relevance of this observation, we conducted luciferase reporter gene assays. HEK293T cells were co-transfected with pGL3-promoter-3xMEF2s, pRL-TK Renilla control vector, and a full-length HDAC4 over-expression vector (WT, F93D or H109D). Compared to cells overexpressing $HDAC4^{WT}$ or $HDAC4^{H109D}$, cells transfected with $HDAC4^{F93D}$ showed an over 1.8-fold increase in luciferase activity (Figure 6C). This observation indicates that the impaired dimerization ability of HDAC4 can interfere with its function in repressing the transcriptional activities of MEF2 family transcription factors. Based on this, it can be inferred that the formation of high-order complexes may lead to an enhancement of HDAC4's activity to repress gene transcription.

Discussion

Crystal structures showed that diverse MEF2 cofactors bind MEF2 through an amphipathic helix, including class IIa HDACs (20,40,43). In addition to this amphipathic MEF2-binding helix, our structure reveals an additional interaction interface between HDAC4 and MEF2A, which is contributed by the loop (residues 152–166) adjacent to the amphipathic helix (Figure 2D). The additional interaction contributes to an ∼430 $Å^2$ binding surface for MEF2-A binding, which is more than half that of the amphipathic helix (720 $Å^2$). Therefore, this interaction interface could further contribute to the recruitment of HDAC4 to MEF2A and the interaction stability. Interestingly, sequence alignment showed that the loop region is highly conserved among class IIa HDAC members (Supplementary Figure S4), suggesting that it may be functionally important in binding with their target transcription factors, including MEF2 proteins.

Previous structural and biochemical studies have demonstrated that residues 130–151 of $HDAC4_{GRD}$ is disordered (17). In our $HDAC4_{GRD}$–$MEF2A_{1–95}$ structure, this region formed an extended helix with a well-defined backbone density. The differences observed between the MEF2A-bound $HDAC4_{GRD}$ and its apo structure may suggest that this region undergoes conformational changes during the assembly of the transcriptional repressor. The flexibility of this region may facilitate the binding of dimeric HDAC4 to MEF2 transcription factors from different orientations and distances, while folding of the helix after assembly may confer the complex rigidity and stability. Similar conformational changes were observed in the STA1T1/P300 and P53/P300 transcriptional regulatory complexes, where the P300-binding motifs of STA1T1 and P53 were disordered in solution and folded into a short helix upon binding by P300 (44,45).

We have shown that the $HDAC4_{GRD}$–$MEF2A_{1–95}$–DNA complex presents as a monomer at a low $HDAC4_{GRD}$ concentration by EMSA. Strikingly, once the concentration of $HDAC4_{GRD}$ increased, both free DNA and the monomeric complex band disappeared while no additional upper bands were observed, indicating that higher-order complexes may have been formed but failed to enter the 6% EMSA gel. We tried to extend the electrophoresis time in an attempt to drive the higher-order $HDAC4_{GRD}$–$MEF2A_{1–95}$–DNA complexes into the gel but without success. A possible explanation could be that the migratory orientation of the $HDAC4_{GRD}$–$MEF2A_{1–95}$–DNA monomer is along the long axis. In contrast, it is perpendicular to the long axis when more than one DNA molecule is bound by the dimeric or higher-order complex. Once the migration orientation is perpendicular to the long helix, such a 27 nm in-length complex may be too large to pass through the gel matrix.

Combined with biochemical, AFM, and cell-based functional assays, it has become clear now that HDAC4 utilizes interface I to dimerize and bridge two separate MEF2A–DNA complexes. Crystal packing analysis suggests that interface II may also serve as a potential HDAC4–HDAC4 interaction interface. Although our mutagenesis assays demonstrated that the mutation of interface II residue H109 did not disrupt the HDAC4-dimerization ability, it is still possible that the dimeric HDAC4–MEF2A–DNA complexes could utilize this interface to form a tetramer or higher-order complex (Supplementary Figure S5A). Interestingly, our previous study showed that apo $HDAC4_{GRD}$ can form a tetramer, which can be regarded as two dimeric $HDAC4_{GRD}$ molecules further dimerizing at an approximate cross angle of 20° (17) (Supplementary Figure S3A). However, when we assigned two dimeric $HDAC4_{GRD}$–$MEF2A_{1–95}$–DNA complexes at the same orientation, clashes were observed at residues 130–155 of $HDAC4_{GRD}$ (Supplementary Figure S5B). This partially explains why these residues of $HDAC4_{GRD}$ are disordered in the crystal structure of the apo $HDAC4_{GRD}$ tetramer. Therefore, we speculate that HDAC4, upon binding with MEF2A proteins, may not adopt such a tetrameric mode as its apo forms.

It is increasingly recognized that long-range chromatin interactions play an essential role in transcriptional regulation (26,46,47). Many transcription factors have been reported to be involved in DNA bridging, such as FOXP3, GATA3 and MEF2 proteins (Figure 7A-D). FOXP3 has been shown to mediate DNA bridging by forming a domain-swapped homod-

imer (48). GATA3 possesses a tandem of two zinc fingers (the N- and C-fingers) capable of binding two separate DNA sites simultaneously. The link region between the N- and C-finger may confer GATA3 high flexibility in various modes of DNA binding and DNA bridging (49). Distinct from GATA3 and FOXP3, MEF2 transcription factors develop a DNA bridging mechanism by recruiting other cofactors. The binding of different cofactors confers MEF2 with different transcription activities and diverse genomic interactions. For example, P300 binds three MEF2–DNA complexes and acts as a coactivator (43), while class IIa HDACs can bridge two MEF2–DNA complexes to repress their transcription activities. The dimerization of the HDAC–MEF2A complex may confer its ability to bridge two separate DNA sites and induce a transcriptionally repressive chromatin conformation by pulling together two distal genomic loci from either the same or different chromosomes (Figure 7D and E). As has been discussed above, the HDAC4–MEF2A–DNA complex may further dimerize to construct a higher-order chromatin conformation (Figure 7E).

Previous studies have shown that the N-terminal fragment of HDAC4 (residues 1–208) and MEF2 bind each other to form spherical punctate nuclear bodies (7), now commonly known as phase separation or subnuclear condensates (50). Interestingly, HDAC4 (1–208) alone showed a pan-cellular distribution, whereas MEF2 alone showed a pan-nuclear distribution. When co-expressed, MEF2 induces nuclear translocation of HDAC4 (1–208) and the formation of punctate nuclear bodies. The assembly of the HDAC4–MEF2–DNA complex presented here could serve as the nucleation event of the phase separation and the formation of the subnuclear condensates.

In summary, we showed that the $HDAC4_{GRD}$–$MEF2A_{1–95}$–DNA complex could assemble into a higher-order structure by both biochemical and crystallography studies. Further cell-based luciferase reporter gene assays demonstrated that the formation of the high-order HDAC4 complex is important for its function in repressing the transcriptional activities of MEF2 proteins. Our studies reveal the first high-order structural model of site-specific recruitment of class IIa HDACs by the MEF2 transcription factor and provide new insights into long-range gene regulation mediated by the HDAC4–MEF2 axis.

Data availability

Atomic coordinate and structural factor for the HDAC4–MEF2A–DNA complex have been deposited in the Protein Data Bank under accession code 7XUZ.

Supplementary data

Supplementary Data are available at NAR Online.

Acknowledgements

We thank the staff from the Advanced Light Source beamline 8.2.1 for assistance during diffraction data collection. We also thank the staff from the National Center for Protein Science (Shanghai) for assistance with AFM sample preparation and imaging.

Funding

National Natural Science Foundation of China [81974074, 82172654]; Hunan Provincial Science and Technology Department [2018RS3026, 2021RC4012]; China Postdoctoral Science Foundation [2021M693574]; Science and Technology Innovation Program of Hunan Province [2021RC2034]; Youth Science Foundation of Xiangya Hospital [2021Q15]; National Institutes of Health Grants [R01 HL076334, R01 GM064642]. Funding for open access charge: Science and Technology Innovation Program of Hunan Province [2021RC2034].

Conflict of interest statement

None declared.

References

1. Haberland,M., Montgomery,R.L. and Olson,E.N. (2009) The many roles of histone deacetylases in development and physiology: implications for disease and therapy. *Nat. Rev. Genet.*, **10**, 32–42.
2. Ruthenburg,A.J., Li,H., Patel,D.J. and Allis,C.D. (2007) Multivalent engagement of chromatin modifications by linked binding modules. *Nat. Rev. Mol. Cell Biol.*, **8**, 983–994.
3. Grunstein,M. (1997) Histone acetylation in chromatin structure and transcription. *Nature*, **389**, 349–352.
4. Parra,M. (2015) Class IIa HDACs - new insights into their functions in physiology and pathology. *FEBS J.*, **282**, 1736–1744.
5. Verdin,E., Dequiedt,F., Kasler,H.G., Verdin,E., Dequiedt,F. and Kasler (2003) HGClass II histone deacetylases: versatile regulators. *Trends Genet.*, **19**, 286–293.
6. Lahm,A., Paolini,C., Pallaoro,M., Nardi,M.C., Jones,P., Neddermann,P., Sambucini,S., Bottomley,M.J., Lo Surdo,P., Carfí,A., *et al.* (2007) Unraveling the hidden catalytic activity of vertebrate class IIa histone deacetylases. *Proc. Natl. Acad. Sci. U.S.A.*, **104**, 17335–17340.
7. Chan,J.K., Sun,L., Yang,X.J., Zhu,G. and Wu,Z. (2003) Functional characterization of an amino-terminal region of HDAC4 that possesses MEF2 binding and transcriptional repressive activity. *J. Biol. Chem.*, **278**, 23515–23521.
8. Sparrow,D.B., Miska,E.A., Langley,E., Reynaud-Deonauth,S., Kotecha,S., Towers,N., Spohr,G., Kouzarides,T. and Mohun,T.J. (1999) MEF-2 function is modified by a novel co-repressor, MITR. *EMBO J.*, **18**, 5085–5098.
9. Di,G.E. and Brancolini,C. (2016) Regulation of class IIa HDAC activities: it is not only matter of subcellular localization. *Epigenomics*, **8**, 251–269.
10. Lu,J., McKinsey,T.A., Zhang,C.L. and Olson,E.N. (2000) Regulation of skeletal myogenesis by association of the MEF2 transcription factor with class II histone deacetylases. *Mol. Cell*, **6**, 233–244.
11. Verdin,E., Dequiedt,F. and Kasler,H.G. (2003) Class II histone deacetylases: versatile regulators. *Trends Genet.*, **19**, 286–293.
12. Cohen,T.J., Barrientos,T., Hartman,Z.C., Garvey,S.M., Cox,G.A. and Yao,T.P. (2009) The deacetylase HDAC4 controls myocyte enhancing factor-2-dependent structural gene expression in response to neural activity. *FASEB J.*, **23**, 99–106.
13. Di Giorgio,E., Hancock,W.W. and Brancolini,C. (2018) MEF2 and the tumorigenic process, hic sunt leones. *Biochim. Biophys Acta Rev. Cancer*, **1870**, 261–273.
14. Clocchiatti,A., Florean,C. and Brancolini,C. (2011) Class IIa HDACs: from important roles in differentiation to possible implications in tumourigenesis. *J. Cell. Mol. Med.*, **15**, 1833–1846.
15. Clocchiatti,A., Di Giorgio,E., Ingrao,S., Meyer-Almes,F.J., Tripodo,C. and Brancolini,C. (2013) Class IIa HDACs repressive activities on MEF2-depedent transcription are associated with poor prognosis of ER^+ breast tumors. *FASEB J.*, **27**, 942–954.

16. Schwieger,M., Schüler,A., Forster,M., Engelmann,A., Arnold,M.A., Delwel,R., Valk,P.J., Löhler,J., Slany,R.K., Olson,E.N., *et al.* (2009) Homing and invasiveness of MLL/ENL leukemic cells is regulated by MEF2C. *Blood*, **114**, 2476–2488.
17. Guo,L., Han,A., Bates,D.L., Cao,J. and Chen,L. (2007) Crystal structure of a conserved N-terminal domain of histone deacetylase 4 reveals functional insights into glutamine-rich domains. *Proc. Natl. Acad. Sci. U.S.A.*, **104**, 4297–4302.
18. Molkentin,J.D., Black,B.L., Martin,J.F. and Olson,E.N. (1996) Mutational analysis of the DNA binding, dimerization, and transcriptional activation domains of MEF2C. *Mol. Cell. Biol.*, **16**, 2627–2636.
19. Wu,Y., Dey,R., Han,A., Jayathilaka,N., Philips,M., Ye,J. and Chen,L. (2010) Structure of the MADS-box/MEF2 domain of MEF2A bound to DNA and its implication for myocardin recruitment. *J. Mol. Biol.*, **397**, 520–533.
20. Han,A., He,J., Wu,Y., Liu,J.O. and Chen,L. (2005) Mechanism of recruitment of class II histone deacetylases by myocyte enhancer factor-2. *J. Mol. Biol.*, **345**, 91–102.
21. Potthoff,M.J. and Olson,E.N. (2007) MEF2: a central regulator of diverse developmental programs. *Development*, **134**, 4131–4140.
22. Zhang,C.L., McKinsey,T.A., Lu,J.R. and Olson,E.N. (2001) Association of COOH-terminal-binding protein (CtBP) and MEF2-interacting transcription repressor (MITR) contributes to transcriptional repression of the MEF2 transcription factor. *J. Biol. Chem.*, **276**, 35–39.
23. Zhang,C.L., Mckinsey,T.A., Lu,J.R. and Olson,E.N. (2001) Association of COOH-terminal-binding protein (CtBP) and MEF2-interacting transcription repressor (MITR) contributes to transcriptional repression of the MEF2 transcription factor. *J. Biol. Chem.*, **276**, 35–39.
24. Kong,X. and Sawalha,A.H. (2019) Takayasu arteritis risk locus in IL6 represses the anti-inflammatory gene GPNMB through chromatin looping and recruiting MEF2-HDAC complex. *Ann. Rheum. Dis.*, **78**, 1388–1397.
25. Di Giorgio,E., Dalla,E., Franforte,E., Paluvai,H., Minisini,M., Trevisanut,M., Picco,R. and Brancolini,C. (2020) Different class IIa HDACs repressive complexes regulate specific epigenetic responses related to cell survival in leiomyosarcoma cells. *Nucleic Acids Res.*, **48**, 646–664.
26. Dekker,J., Rippe,K., Dekker,M. and Kleckner,N. (2002) Capturing chromosome conformation. *Science*, **295**, 1306–1311.
27. Spilianakis,C.G. and Flavell,R.A. (2004) Long-range intrachromosomal interactions in the T helper type 2 cytokine locus. *Nat. Immunol.*, **5**, 1017–1027.
28. Spilianakis,C.G., Lalioti,M.D., Town,T., Lee,G.R. and Flavell,R.A. (2005) Interchromosomal associations between alternatively expressed loci. *Nature*, **435**, 637–645.
29. Jhunjhunwala,S., van Zelm,M.C., Peak,M.M., Cutchin,S., Riblet,R., van Dongen,J.J., Grosveld,F.G., Knoch,T.A. and Murre,C. (2008) The 3D structure of the immunoglobulin heavy-chain locus: implications for long-range genomic interactions. *Cell*, **133**, 265–279.
30. Heidari,N., Phanstiel,D.H., He,C., Grubert,F., Jahanbani,F., Kasowski,M., Zhang,M.Q. and Snyder,M.P. (2014) Genome-wide map of regulatory interactions in the human genome. *Genome Res.*, **24**, 1905–1917.
31. Sandmann,T., Jensen,L.J., Jakobsen,J.S., Karzynski,M.M., Eichenlaub,M.P., Bork,P. and Furlong,E.E. (2006) A temporal map of transcription factor activity: mef2 directly regulates target genes at all stages of muscle development. *Dev. Cell*, **10**, 797–807.
32. Chen,X., Wei,H., Li,J., Liang,X., Dai,S., Jiang,L., Guo,M., Qu,L., Chen,Z., Chen,L., *et al.* (2019) Structural basis for DNA recognition by FOXC2. *Nucleic Acids Res.*, **47**, 3752–3764.
33. Minor,W., Cymborowski,M., Otwinowski,Z. and Chruszcz,M. (2010) HKL-3000: the integration of data reduction and structure solution – from diffraction images to an initial model in minutes. *Acta Crystallogr.*, **62**, 859–866.
34. Mccoy,A.J., Grossekunstleve,R.W., Adams,P.D., Winn,M.D., Storoni,L.C. and Read,R.J. (2007) Phaser crystallographic software. *J. Appl. Crystallogr.*, **40**, 658–674.
35. Terwilliger,T.C., Grosse-Kunstleve,R.W., Afonine,P.V., Moriarty,N.W., Zwart,P.H., Hung,L.W., Read,R.J. and Adams,P.D. (2008) Iterative model building, structure refinement and density modification with the PHENIX AutoBuild wizard. *Acta. Crystallogr. D Biol. Crystallogr.*, **64**, 61–69.
36. Emsley,P. and Cowtan,K. (2004) Coot: model-building tools for molecular graphics. *Acta. Crystallogr. D Biol. Crystallogr.*, **60**, 2126–2132.
37. Kovalevskiy,O., Nicholls,R.A. and Murshudov,G.N. (2016) Automated refinement of macromolecular structures at low resolution using prior information. *Acta Crystallogr. D Struct. Biol.*, **72**, 1149–1161.
38. Afonine,P.V., Grosse-Kunstleve,R.W., Echols,N., Headd,J.J., Moriarty,N.W., Mustyakimov,M., Terwilliger,T.C., Urzhumtsev,A., Zwart,P.H. and Adams,P.D. (2012) Towards automated crystallographic structure refinement with phenix.Refine. *Acta. Crystallogr. D Biol. Crystallogr.*, **68**, 352–367.
39. Li,J., Dantas Machado,A.C., Guo,M., Sagendorf,J.M., Zhou,Z., Jiang,L., Chen,X., Wu,D., Qu,L., Chen,Z., *et al.* (2017) Structure of the forkhead domain of FOXA2 bound to a complete DNA consensus site. *Biochemistry*, **56**, 3745–3753.
40. Han,A., Pan,F., Stroud,J.C., Youn,H.D., Liu,J.O. and Chen,L. (2003) Sequence-specific recruitment of transcriptional co-repressor Cabin1 by myocyte enhancer factor-2. *Nature*, **422**, 730–734.
41. Krissinel,E. and Henrick,K. (2007) Inference of macromolecular assemblies from crystalline state. *J. Mol. Biol.*, **372**, 774–797.
42. Anderson,C.M., Hu,J., Thomas,R., Gainous,T.B., Celona,B., Sinha,T., Dickel,D.E., Heidt,A.B., Xu,S.M., Bruneau,B.G., *et al.* (2017) Cooperative activation of cardiac transcription through myocardin bridging of paired MEF2 sites. *Development*, **144**, 1235–1241.
43. He,J., Ye,J., Cai,Y., Riquelme,C., Liu,J.O., Liu,X., Han,A. and Chen,L. (2011) Structure of p300 bound to MEF2 on DNA reveals a mechanism of enhanceosome assembly. *Nucleic Acids Res.*, **39**, 4464–4474.
44. Feng,H., Jenkins,L.M.M., Durell,S.R., Hayashi,R., Mazur,S.J., Cherry,S., Tropea,J.E., Miller,M., Wlodawer,A. and Appella,E. (2009) Structural basis for p300 Taz2/p53 TAD1 binding and modulation by phosphorylation. *Structure*, **17**, 202–210.
45. Wojciak,J.M., Martinez-Yamout,M.A., Dyson,H.J. and Wright,P.E. (2009) Structural basis for recruitment of CBP/p300 coactivators by STAT1 and STAT2 transactivation domains. *EMBO J.*, **28**, 948–958.
46. Lieberman-Aiden,E., van Berkum,N.L., Williams,L., Imakaev,M., Ragoczy,T., Telling,A., Amit,I., Lajoie,B.R., Sabo,P.J., Dorschner,M.O., *et al.* (2009) Comprehensive mapping of long-range interactions reveals folding principles of the human genome. *Science*, **326**, 289–293.
47. Dixon,J.R., Selvaraj,S., Yue,F., Kim,A., Li,Y., Shen,Y., Hu,M., Liu,J.S. and Ren,B. (2012) Topological domains in mammalian genomes identified by analysis of chromatin interactions. *Nature*, **485**, 376–380.
48. Chen,Y., Chen,C., Zhang,Z., Liu,C.C., Johnson,M.E., Espinoza,C.A., Edsall,L.E., Ren,B., Zhou,X.J., Grant,S.F., *et al.* (2015) DNA binding by FOXP3 domain-swapped dimer suggests mechanisms of long-range chromosomal interactions. *Nucleic Acids Res.*, **43**, 1268–1282.
49. Chen,Y., Bates,D.L., Dey,R., Chen,P.H., Machado,A.C., Laird-Offringa,I.A., Rohs,R. and Chen,L. (2012) DNA binding by GATA transcription factor suggests mechanisms of DNA looping and long-range gene regulation. *Cell Rep.*, **2**, 1197–1206.
50. Bhat,P., Honson,D. and Guttman,M. (2021) Nuclear compartmentalization as a mechanism of quantitative control of gene expression. *Nat. Rev. Mol. Cell Biol.*, **22**, 653–670.

Received: July 27, 2023. **Revised:** December 1, 2023. **Editorial Decision:** January 4, 2024. **Accepted:** January 10, 2024